Oscillatory instability of a three-dimensional lid-driven flow in a cube

Yuri Feldman[a] and Alexander Yu. Gelfgat
School of Mechanical Engineering, Faculty of Engineering, Tel-Aviv University, Ramat, Aviv 69978, Israel

(Received 10 November 2009; accepted 3 August 2010; published online 30 September 2010)

A series of time-dependent three-dimensional (3D) computations of a lid-driven flow in a cube with no-slip boundaries is performed to find the critical Reynolds number corresponding to the steady-oscillatory transition. The computations are done in a fully coupled pressure-velocity formulation on 104^3, 152^3, and 200^3 stretched grids. Grid-independence of the results is established. It is found that the oscillatory instability of the flow sets in via a subcritical symmetry-breaking Hopf bifurcation at $\mathrm{Re}_{cr} \approx 1914$ with the nondimensional frequency $\omega = 0.575$. Three-dimensional patterns in the steady and oscillatory flow regimes are compared with the previously studied two-dimensional configuration and a three-dimensional model with periodic boundary conditions imposed in the spanwise direction. © *2010 American Institute of Physics*. [doi:10.1063/1.3487476]

I. INTRODUCTION

Lid-driven cavity flow is a classical benchmark problem for verification of numerical methods of incompressible fluid dynamics. The problem is known to get harder with increase of the Reynolds number because smaller-scale vortices must be accurately resolved. Ghia *et al.*[1] and Schreiber and Keller[2] were among the first who reported steady flow calculations of benchmark quality. At about the same time, the pioneering works of Burgraf[3] and Pan and Acrivos[4] attracted more interest to confined recirculating flows. Most previous studies, which are not reviewed here, were devoted to the two-dimensional problem. At the same time several early studies, e.g., Refs. 5 and 6, reported the first description of three-dimensional vortical structures and end-wall effects. Later, after grid resolution and numerical accuracy were significantly improved, even more accurate solutions of the two-dimensional problem were obtained, among which one would mention the benchmark quality results computed by spectral methods.[7,8]

The study of the three-dimensional lid-driven cavity flow was started by Davis and Mallinson[9] and Goda.[10] Later, Freitas *et al.*[6] demonstrated the three-dimensional character of the flow, and Koseff and Street[11] pointed out three-dimensional effects near the end-walls of a finite-size system that always exists in a laboratory setup. Other three-dimensional studies focused mainly on numerical techniques and the flow structure topology,[12–19] but did not report results of benchmark quality. The first benchmark-quality solution on the three-dimensional flow at $\mathrm{Re} = 10^3$ was reported by Albensoeder and Kuhlmann.[20] More recently three-dimensional steady flows were computed by Turner *et al.*[21] for Re number up to $\mathrm{Re} = 865$ and by Sun *et al.*[22] for $\mathrm{Re} = 1000$ mainly for the purpose of code verification.

Stability of the lid-driven cavity flow was studied mainly for the two-dimensional configuration, e.g., in Refs. 23–27, yielding $\mathrm{Re}_{cr,2D} \approx 8000$. Being important for two-dimensional (2D) codes benchmarking, these results strongly overestimate the stability limit of a realistic 3D flow. Thus, Ramanan and Homsy[28] and later Theofilis,[29] Albensoeder *et al.*,[30] and Theofilis *et al.*[31] showed that the critical Reynolds number becomes an order of magnitude smaller if three-dimensional perturbations periodic in the third direction are superimposed on the purely two-dimensional flow. An attempt to study three-dimensional flow structures was undertaken in a series of benchmark exercises.[32] However, as was already stated by Albensoeder and Kuhlmann,[20] the results remained inconclusive due to a significant disagreement between numerical solutions obtained by different methods at different resolutions.

After transition to unsteadiness, with further increase of the Reynolds number, the flow becomes turbulent. Only Leiriche and Gavrilakis[33] and Bouffanias *et al.*[34] studied strongly supercritical 3D flows at $\mathrm{Re} = 10^4$ and larger. Stability of flow in a three-dimensional lid-driven cavity was studied only for spatially periodic spanwise boundary conditions,[28,35,36] for which the base flow remains two-dimensional. Beya and Lili[37] investigated three-dimensional incompressible flow in a two-sided nonfacing lid-driven cubical cavity. They observed transition to unsteadiness via a Hopf bifurcation at $\mathrm{Re} \approx 540$. Their periodic solution was obtained on a rather coarse 64^3 grid, which may be insufficient to resolve both the flow and the most unstable eigenvector. To the best of our knowledge, stability of a developed 3D flow in a box all of whose boundaries are no-slip using denser grids (100 and more nodes in the shortest direction) is still a challenge and has not been addressed.

In this study we compute the critical Reynolds number corresponding to the transition to unsteadiness in the lid-driven cubic cavity with no-slip boundaries. The stability results are revealed from a series of time-dependent solutions of the full three-dimensional problem using 104^3, 152^3, and 200^3 stretched grids. The calculations are performed in a fully coupled pressure-velocity formulation using the multigrid technique with the analytical solution accelerated coupled line Gauss–Seidel (ASA-CLGS) smoother.[38] We show that the critical Reynolds number is about two times

[a]Author to whom correspondence should be addressed. Electronic mail: yurifeld@post.tau.ac.il.

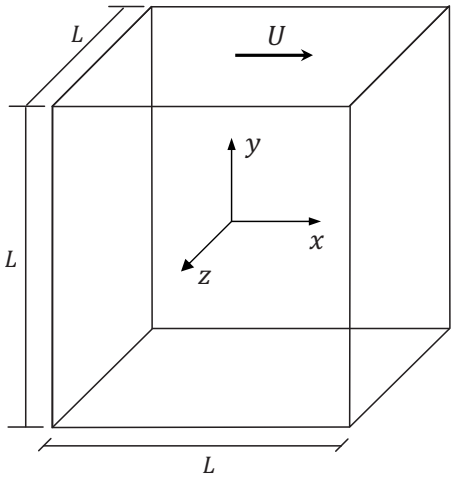

FIG. 1. Lid-driven cavity physical model and coordinate system.

larger than that obtained for the periodic spanwise boundary conditions. However, it is significantly smaller than one corresponding to the two-dimensional model. Applying the Richardson extrapolation we estimate the critical Reynolds number as $\mathrm{Re}_{cr} \approx 1914$. We present arguments showing that the transition to unsteadiness takes place via a subcritical Hopf bifurcation, so that the resulting oscillatory flow looses the symmetry with respect to the cavity midplane.

II. FORMULATION OF THE PROBLEM

A cubic lid-driven cavity with the side of length L is considered. The upper boundary moves with a constant velocity U in the x direction, while all other boundaries are stationary. The no-slip boundary conditions are applied on all the boundaries (see Fig. 1). The flow is described by the continuity and momentum equations,

$$\nabla \cdot \boldsymbol{u} = 0, \tag{1}$$

$$\partial \boldsymbol{u}/\partial t + (\boldsymbol{u} \cdot \nabla)\boldsymbol{u} = -\nabla p + \frac{1}{\mathrm{Re}}\nabla^2 \boldsymbol{u}, \tag{2}$$

where dimensionless variables are velocity $\boldsymbol{u}(u,v,w)$, pressure p, and time t. The equations are rendered dimensionless using the scales L, U, $t=L/U$, and $P=\rho U^2$ for length, velocity, time, and pressure, respectively. Here ρ is the fluid density. The Reynolds number is defined by $\mathrm{Re}=UL/\nu$, where ν is the kinematic viscosity. The flow region is defined in the dimensionless Cartesian coordinates x, y, and z each of which varies between -0.5 and 0.5 (Fig. 1).

III. NUMERICAL METHOD

The numerical technique used in this study is based on a finite volume discretization of the governing equations. The numerical solution is obtained in a fully pressure-velocity coupled formulation using the multigrid with ASA-CLGS smoother. The whole numerical approach is described in Ref. 38. Here we only give some general remarks related to the algorithm convergence and scalability properties in order to outline the ability of our approach to reveal the critical Reynolds numbers by performing fully three-dimensional time-dependent calculations.

The main feature of the ASA-CLGS smoother, which drastically increases the algorithm scalability, is the existence of an analytical solution for the entire column (row) of finite volumes characterized by a local computational complexity of $O(5N)$, where N is a total number of pressure and velocity corrections associated with the given column (row).[38] This allows a two-dimensional virtual topology to be used for the three-dimensional configuration where each CPU is responsible for its subdomain consisting of $L \times M$ columns in x and z directions, respectively. Using a staggered grid together with the smoother based on a block Gauss–Seidel iteration limits, the minimal subdomain dimension to 3×3. This fact together with the resolution of the multigrid coarsest grid determines the maximum number of CPU cores that may be involved in the analysis for a certain grid. Thus, the maximum number of cores is restricted mainly by a resolution of the coarsest grid. Therefore, the general strategy of the analysis is to use the multigrid approach only when going from the steady state to the oscillatory regime, by rapidly increasing Re. Once the oscillatory regime is reached and changes between two consecutive time steps for all variables become very small, the calculations are performed only on the finest grid, which is done on the maximum possible number of CPU cores. Note that the number of cores is taken to be a power of 2 to yield the highest efficiency of a massively parallel platform. The characteristic times needed to perform a single time step using 1024 Intel Xeon Gainestown CPUs are 25.7, 47, and 66.9 ms for the 104^3, 152^3, and 200^3 grids, respectively. It should be noted, however, that these values may vary depending on number of iterations needed to reach convergence.

IV. RESULTS AND DISCUSSION

A. Steady flows

The steady state results were obtained for Reynolds numbers 10^3, 1.5×10^3, and 1.9×10^3 using stretched staggered grids with an equal number of finite volumes in each direction 104, 152, or 200. The zero-grid-step limit of the results was then calculated using Richardson extrapolation for each pair of grids. We observed that the results of Richardson extrapolation based on the 104^3 and 152^3 grids and on the 152^3 and 200^3 grids coincide to three decimal places. This allows us to conclude that the asymptotic $O(h^2)$ grid convergence is reached. Steady velocity and pressure profiles are reported in Figs. 2–4, where symbols correspond to the data obtained exactly at points reported in the Table V of Ref. 20. Note that the calculated steady state flow at $\mathrm{Re}=10^3$ compares well with the results of Albensoeder and Kuhlmann[20] (Fig. 2). Good agreement is observed for the whole range of the center line velocity and pressure values, which verifies the present calculations.

Figure 3 compares steady state velocity and pressure profiles along the centerlines $(x,0,0)$ and $(0,y,0)$ for $\mathrm{Re}=10^3$, 1.5×10^3, and 1.9×10^3. With increase in Reynolds number, the dimensionless velocity components (normalized

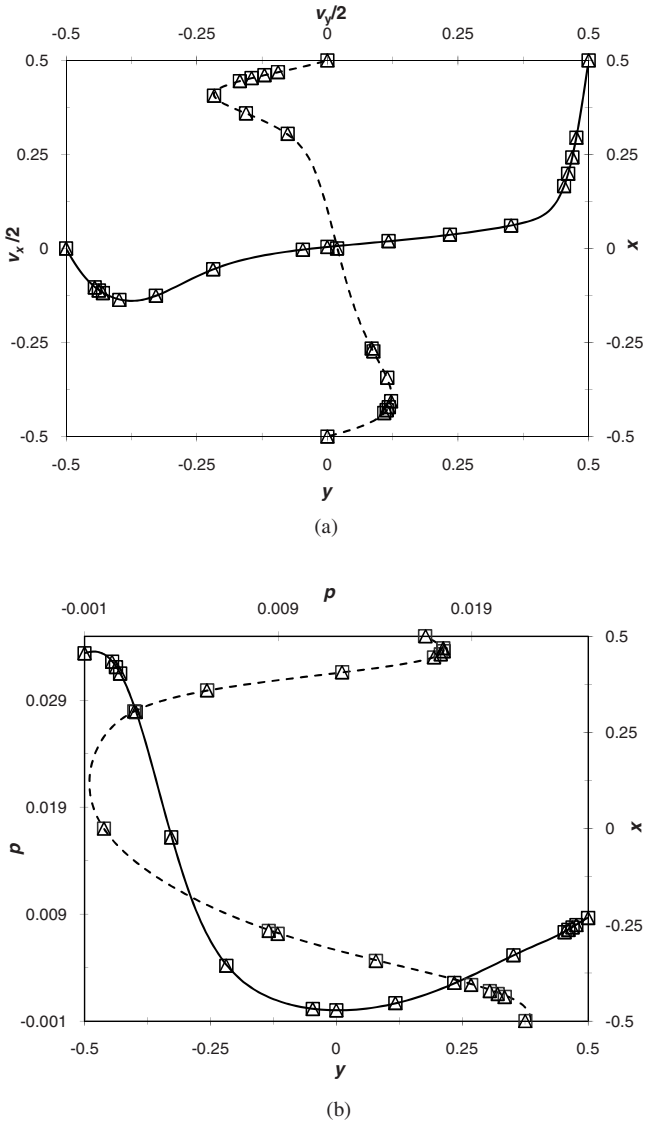

FIG. 2. Comparison between the present solution (△) (Richardson extrapolation for 152^3 and 200^3 grids) and the solution of Albensoeder and Kuhlmann (Ref. 20) (□), $\mathrm{Re}=10^3$: (a) $v_x/2$ and $v_y/2$ velocity components along centerlines $(0,y,0)$: solid line; $(x,0,0)$: dashed line. (b) Pressure p along centerline $(0,y,0)$: solid line; $(x,0,0)$: dashed line.

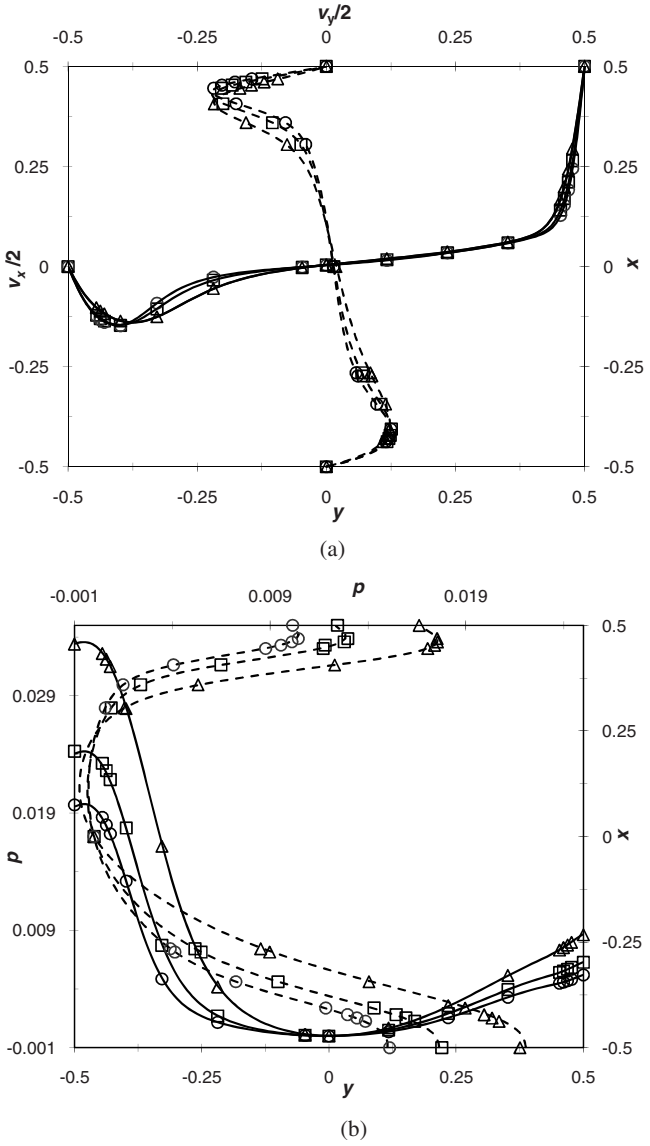

FIG. 3. Steady state flow profiles obtained by Richardson extrapolation for 152^3 and 200^3 grids for $\mathrm{Re}=10^3$ (△), $\mathrm{Re}=1.5\times10^3$ (□), and $\mathrm{Re}=1.9\times10^3$ (○): (a) $v_x/2$ and $v_y/2$ velocity components along centerlines $(0,y,0)$: solid line; $(x,0,0)$: dashed line. (b) Pressure p along centerline $(0,y,0)$: solid line; $(x,0,0)$: dashed line.

by the lid velocity) do not change significantly [Fig. 3(a)], while the pressure values undergo a noticeable change. Thus, near the center of the cavity bottom and at the left and right boundaries, the difference between the pressure values for $\mathrm{Re}=10^3$ and $\mathrm{Re}=1.9\times10^3$ exceeds 50% [see Fig. 3(b)].

Computations for $\mathrm{Re}\leq1.9\times10^3$ showed that the steady flow state remains stable and symmetric with respect to reflection in the cavity midplane $z=0$, which is a clear sequence of the symmetric problem geometry. An illustration is presented in Fig. 4, where $v_z(z)$ profiles are shown for $\mathrm{Re}=1.5\times10^3$. Note that the z direction is orthogonal to the main circulation plane and corresponds to the spanwise coordinate of the two-dimensional problem (Fig. 1). The three profiles correspond to the lines passing through centers of the primary and two secondary eddies [see Fig. 5(a)]. As expected, all profiles are antisymmetric with respect to the cavity midplane $z=0$, where z-velocity is zero. This means, in particular, that in the case of steady flow fluid particles located in the midplane $z=0$ never leave it. At the same time, the particles located close to the midplane near the centers of the main and secondary eddies attain a significant motion in z direction [Figs. 5(b) and 5(c)]. It is seen that in the vicinity of eddy centers, the particles exhibit a spiraling motion. One observes that in the (x, y) plane the particles spiral outward from the main eddy center [Fig. 5(b)] and tend to flow "inside" it from both spanwise directions. Both secondary eddies located in the right and left lower corners [Fig. 5(c)] are characterized by a spiraling motion toward the eddy centers, while the fluid tends to leave the centers in both spanwise directions. The appearance of flow in the spanwise direction is a clear effect of the no-slip boundaries $z=\pm0.5$. The drop in the x- and y-velocity values between the midplane and the boundaries necessarily leads to the appearance of a nonzero z-component of pressure gradient, which, in turn, drives the

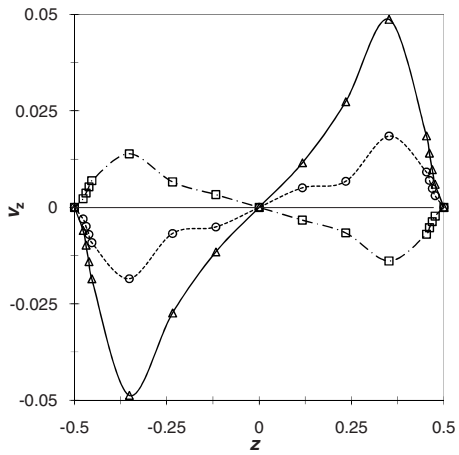

FIG. 4. v_z component profiles for $\mathrm{Re}=1.5\times10^3$ along three lines going through the center of downstream secondary vortex (△) (0.3905, −0.398, 0), primary vortex (□) (0.1, −0.035, 0), and upstream secondary vortex (○) (−0.454, −0.4165, 0).

flow in the z direction. The latter represents a qualitative difference between two- and three-dimensional configurations when flow near the midplane is compared with the 2D model. Note that since v_z is an odd function of z, the derivatives $\partial v_z/\partial z$ do not vanish at the midplane (Fig. 4), which necessarily means that other velocity components at the midplane flow do not coincide in 2D and 3D models, in spite of the zero v_z value. In general, when all boundaries are no-slip, all three velocity components are nonzero, which, in particular, as is shown in Sec. IV B, strongly affects the flow stability properties.

B. Transition to unsteadiness and oscillatory flow regimes

In the following we assume that transition to unsteadiness takes place via a Hopf bifurcation at $\mathrm{Re}=\mathrm{Re}_{\mathrm{cr}}$. This means that at $\mathrm{Re}=\mathrm{Re}_{\mathrm{cr}}$ the spectrum of the problem linearized about the steady state contains a single pair of leading eigenvalues $\sigma\pm i\omega_{\mathrm{cr}}$, whose real part σ crosses the zero value. Apparently, $\sigma<0$ corresponds to subcritical flows at $\mathrm{Re}<\mathrm{Re}_{\mathrm{cr}}$ and $\sigma>0$ to supercritical flows at $\mathrm{Re}>\mathrm{Re}_{\mathrm{cr}}$. If, additionally, at $\mathrm{Re}=\mathrm{Re}_{\mathrm{cr}}$ $(\partial\sigma/\partial\mathrm{Re})\neq0$, the conditions of the Hopf theorem hold and the flow in the vicinity of bifurcation point can be described as[39]

$$\mathbf{v}(t,\mathrm{Re})=\mathbf{v}_0(\mathrm{Re}_{\mathrm{cr}})+\varepsilon\mathrm{Real}[\mathbf{V}\exp(i\omega t)]+O(\varepsilon^2), \tag{3}$$

where $\mathbf{v}_0(\mathrm{Re}_{\mathrm{cr}})$ is the steady state at the critical point and $\mathbf{V}$ is the eigenvector corresponding to the leading eigenvalue $\lambda=i\omega_{\mathrm{cr}}$. In the case of supercritical Hopf bifurcation, the oscillation amplitude ε, as well as the deviation of the oscillations frequency from its critical value $\omega-\omega_{\mathrm{cr}}$, is proportional to $\sqrt{\mathrm{Re}-\mathrm{Re}_{\mathrm{cr}}}$ (see Ref. 39). The dependence $\varepsilon\sim\sqrt{\mathrm{Re}-\mathrm{Re}_{\mathrm{cr}}}$ yields a convenient way to estimate $\mathrm{Re}_{\mathrm{cr}}$ from a sequence of oscillation amplitudes of several slightly supercritical flows. Our calculations for the problem considered here revealed a sudden increase of the oscillation amplitude from slowly decaying at $\mathrm{Re}<\mathrm{Re}_{\mathrm{cr}}$ to a finite value at $\mathrm{Re}>\mathrm{Re}_{\mathrm{cr}}$. This is evidence for the subcritical bifurcation for which Eq. (3) describes an unstable solution branch for $\mathrm{Re}<\mathrm{Re}_{\mathrm{cr}}$, which

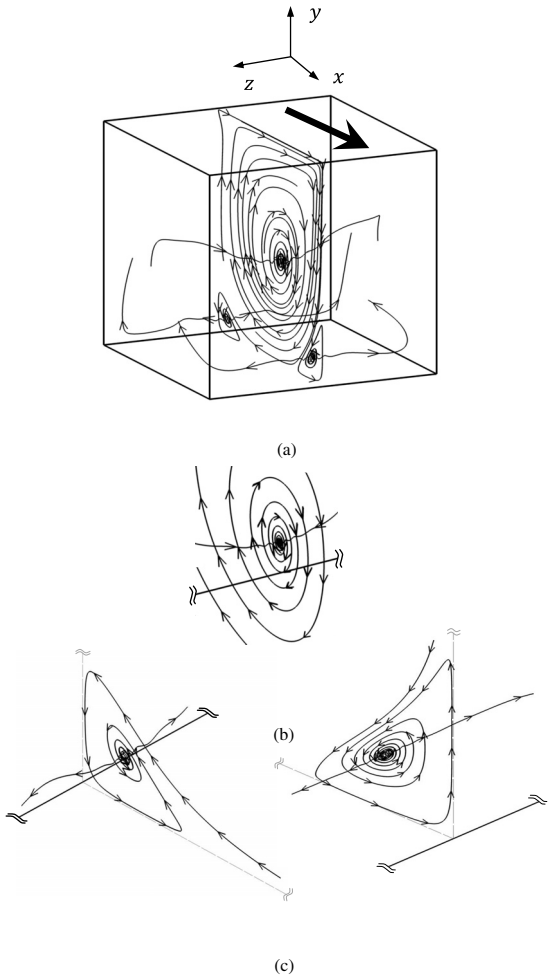

FIG. 5. Three-dimensional structure of three main flow eddies: (a) general view; (b) primary eddy; (c) left and right secondary eddies. The lid motion is indicated by the arrow.

cannot be obtained via the time-dependent computations. Thus, to estimate the critical Reynolds number, we cannot rely on the amplitude growth rates and can use only a series of calculations corresponding to subcritical flow regimes that exhibit oscillations with decaying amplitudes. Thus, assuming that the oscillations of a function $f(t)$ decay proportionally to $\exp[(\sigma+i\omega)t]$, $\sigma<0$, one can calculate the value of σ as

$$\sigma=\frac{\ln[f(t_k)/f(t_{k-1})]}{t_k-t_{k-1}}, \tag{4}$$

where t_k denotes the instants of time at which $f(t)$ has local maxima, i.e., $f'(t_k)=0$, $f''(t_k)<0$ for $k=1,2,3,\ldots$. Calculating values of σ for two subcritical values of Re, we obtain the value of $\mathrm{Re}_{\mathrm{cr}}$ by extrapolating σ to zero. Clearly, the times t_k must be long enough, so that all the disturbance modes except the most dangerous one will have already decayed to zero. Table I shows amplitude maxima at different times and decay rates σ calculated using Eq. (4). One observes that the decay rates are accurate in the third decimal digit, which makes us confident in the following estimation of $\mathrm{Re}_{\mathrm{cr}}$.

TABLE I. Estimation of critical Reynolds number Re_{cr}.

Grid resolution			Re_{cr}	Richardson extrapolation
	Re=1925	Re=1955		
104^3	$\sigma=-3.99\times10^{-3}$	$\sigma=-4.12\times10^{-4}$	1958	
	$\omega=0.575$	$\omega=0.575$		$Re_{cr}=1919$
	Re=1900	Re=1925		
152^3	$\sigma=-4.41\times10^{-3}$	$\sigma=-1.44\times10^{-3}$	1937	
	$\omega=0.575$	$\omega=0.575$		
	Re=1900	Re=1925		$Re_{cr}=1914$
200^3	$\sigma=-3.36\times10^{-3}$	$\sigma=-2.81\times10^{-4}$	1927	
	$\omega=0.575$	$\omega=0.575$		

Figure 6 illustrates a typical temporal evolution of v_x at a fixed spatial point, which is shown as the deviation from the steady state solution $v_x^{(0)}$ calculated at the same Reynolds number, Re=1900, on a 200^3 grid. The point (−0.34, −0.345, 0), at which the signal is monitored, is chosen close to the location of maximum v_x amplitude (see Fig. 10). Fourier analysis of the signal shows that the oscillations are characterized by a single dimensionless angular frequency ω equal to 0.575 [Fig. 6(b)]. Since only one frequency is observed in the spectrum, we conclude that all disturbance modes except the leading one have decayed sufficiently, so that Eq. (4) can be used for calculation of decaying rate of the leading eigenmode. One observes an exponential decay of the amplitude of oscillation estimated as $\sim e^{-3.36\times10^{-3}t}$ [Fig. 6(a)]. The same time evolution signal obtained for Re=1925 results in the exponential decay estimated as $\sim e^{-2.81\times10^{-4}t}$. The oscillation frequency remains single and its value remains unchanged, which supports our assumption about the Hopf bifurcation. The critical Reynolds number Re_{cr}, corresponding to the transition from steady to periodic regime, was then estimated by linear extrapolation of σ to zero, which yielded $Re_{cr,N=200}=1927$. The same procedure was performed for the 104^3 and 152^3 grids and resulted in the estimates yielded $Re_{cr,N=152}=1937$ and $Re_{cr,N=104}=1958$. To improve the estimation of Re_{cr} at a certain grid, we use at least one Reynolds number located very close (in the range of 0.5%) to the estimated critical value (Table I). Following results in Ref. 40, which showed that it is possible to estimate correctly critical numbers by Richardson extrapolation, we extrapolate the estimated grid-dependent critical values to the zero grid step using both pairs of grids, i.e., for 104^3 and 152^3, and 152^3 and 200^3. This yields almost identical values 1919 and 1914, respectively. Therefore, we conclude that the critical Reynolds number can be estimated as $Re_{cr}\approx1914$ to three decimal places. The estimates of Re_{cr} are summarized in Table I. It is emphasized also that the dimensionless oscillation frequency was equal to 0.575 in all computations independent of the grid and the Reynolds number. Note, that the time scale is L/U, so that the dimensionless frequency is a linear function of the lid velocity. At the same time, the observed convergence of the frequency value is quite unexpected.

A number of computations have been performed on all grids for $Re<Re_{cr,grid}$ taking the flow snapshot at $Re>Re_{cr,grid}$ as an initial condition. Here $Re_{cr,grid}$ stays for an estimate of the critical Reynolds number done on a certain grid (Table I). These calculations were performed on a 104^3 grid for Re=1945 starting from a snapshot calculated for Re=1970, on a 152^3 grid for Re=1925 starting again from a snapshot calculated at Re=1970, and on a 200^3 grid for Re=1920 starting again from a snapshot calculated at Re=1970. All simulations resulted in oscillatory regimes, thus supporting the assumption about the subcritical character of the bifurcation. It was also found, independent of the grid resolution, that a periodic flow obtained for Re=1970 converges to a steady state when the Re number is abruptly reduced to Re=1900. This estimates the depth of hysteresis of the subcritical bifurcation, which appears not to be very deep.

To provide more evidence for grid convergence, we show the time evolution of the total kinetic energy calculated at Re=1970 for all three grids considered (Fig. 7). It is seen that the period of oscillation remains grid-independent. The maximum deviation between the kinetic energy values cal-

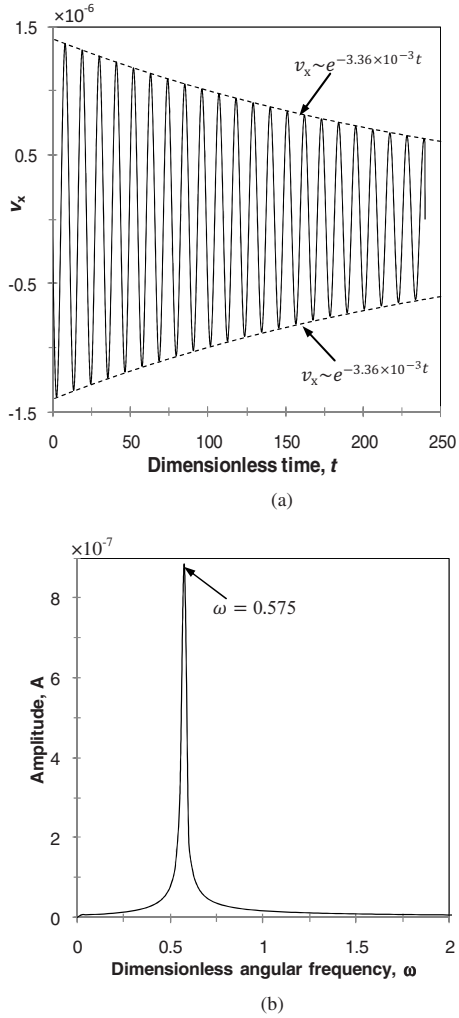

FIG. 6. Typical flow convergence to the steady state, Re=1900, grid 200^3 (a) time dependence of v_x at a control point (−0.34, −0.345, 0); (b) frequency spectrum of the time-dependence shown in frame (a).

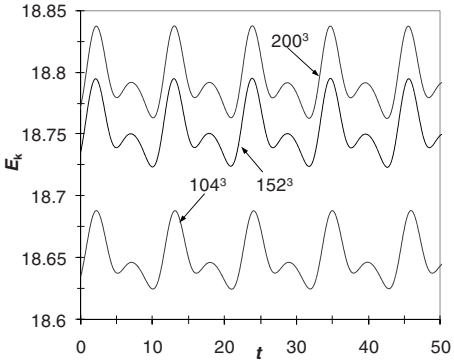

FIG. 7. Typical time evolution of the flow total kinetic energy E_k obtained on 104^3, 152^3, and 200^3 grids corresponding to the oscillatory flow at Re=1970.

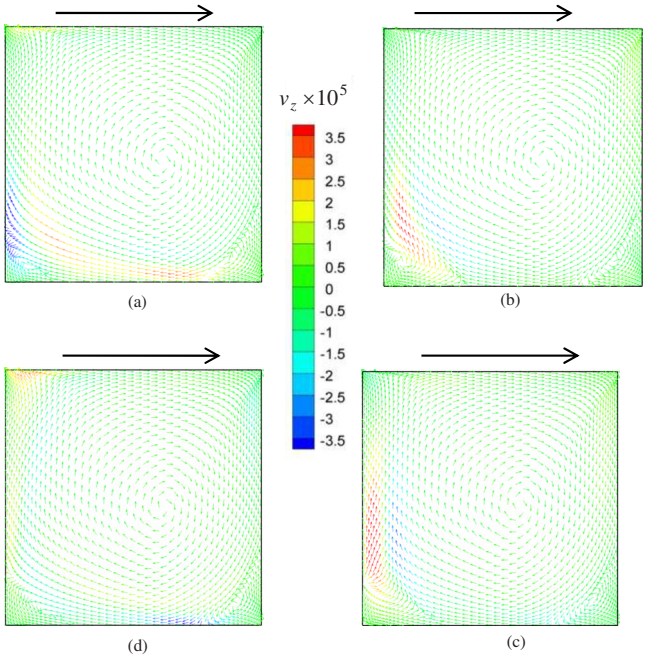

FIG. 8. (Color online) Flow snapshots at the cavity midplane $(x,y,0)$. Colors show the values of a spanwise velocity component v_z. For maxima and minima of $E_k(t)$ shown in Fig. 7: (a) $t=0$ corresponds to a global maximum of the total kinetic energy E_k; (b) $t=2.9$ corresponds to a local minimum of the total kinetic energy E_k; (c) $t=4.8$ corresponds to a local maximum of the total kinetic energy E_k; (d) $t=7.8$ corresponds to a global minimum of the total kinetic energy E_k. The lid motion is indicated by the arrow (enhanced online). [URL: http://dx.doi.org/10.1063/1.3487476.1]

culated on two successive grids decreases with the grid refinement and for the 152^3 and 200^3 grids does not exceed 0.5%.

The spatial pattern of the oscillatory flow is illustrated in Figs. 8–11. Since the patterns are similar for all the grids considered, we use the results obtained on the 104^3 grid for illustration. Figure 8 presents four snapshots of velocity at the cavity midplane $(x,y,0)$. Each snapshot corresponds to the total kinetic energy minimum or maximum value (see Fig. 7): global maximum and minimum in Figs. 8(a) and 8(d) and local maximum and minimum in Figs. 8(b) and 8(c). The colors show values of the spanwise velocity component v_z indicating the three dimensionality of the flow. It is seen that stronger oscillations of v_x and v_z velocity components are located near the boundary $x=-0.5$, while the maximal amplitude of v_y component oscillations is observed near $x=0.5$ boundary. Note also that in the central part of the cross-section, the flow almost does not change. We observe also larger areas with positive values of v_z than with negative ones, which indicates that the reflection symmetry is broken. More details on both observations are given and discussed below.

To provide some quantitative data on the three-dimensional flow oscillations, we present several characteristic profiles of velocity components taken at times corresponding to the maximal and minimal values of the total kinetic energy (Fig. 9). The profiles are plotted along the same lines as for the steady flow in Fig. 2 and additionally in the orthogonal midplane along the centerline $(0,0,z)$. It can be seen that amplitudes of the x- and y-components near the cavity center are small relative to their average values. At the same time the relative amplitude of the spanwise z-component is large while its momentarily values remain small. This observation supports the assumption that, despite their small values, the midplane spanwise velocity may play a significant role in the instability onset.

Qualitative differences in the transition from steady to oscillatory 2D and 3D lid-driven flows can be illustrated additionally by the absolute values of velocity perturbations and amplitudes for two- and three-dimensional configurations, respectively (Fig. 10). Note that the most unstable perturbation is represented by the eigenvector of the linearized problem that corresponds to the leading eigenvalue. Absolute value of the complex eigenvector coincides, to within multiplication by a constant, with the amplitude of a branching oscillatory flow [see Eq. (3)]. This allows us to compare the 2D most unstable perturbation (calculated as the eigenvector of the corresponding linearized problem[8,40]) with the distribution of amplitudes of the developed oscillatory flow. It should be emphasized, however, that because of the subcritical character of the observed 3D bifurcation, the amplitudes reported in Figs. 10(c) and 10(d) do not correspond to the eigenvector. In the 2D case the maximum values of the perturbations of v_x' and v_y' are located close to the cavity upper left corner at the interface between the secondary and primary eddies [Fig. 10(a) and 10(b)]. In the 3D case the transition takes place at significantly lower Re_{cr}, where the secondary upper eddy does not exist yet [Fig. 10(c) and 10(d)]. Moreover, the maximum amplitudes of v_x and v_y are not located close to each other as is observed for the 2D configuration. We observe that maximum amplitudes of oscillation are located between the primary eddy and two different secondary eddies: one located in the lower left corner and another one in the lower right corner, for the amplitudes of v_x and v_y, respectively [Fig. 10(c) and 10(d)]. Thus, for both 2D and 3D configurations the instability causes strong flow oscillations between the main and secondary vortices, as reflected in oscillations shown in Fig. 8. In the case of 3D instability these oscillations are located between the main

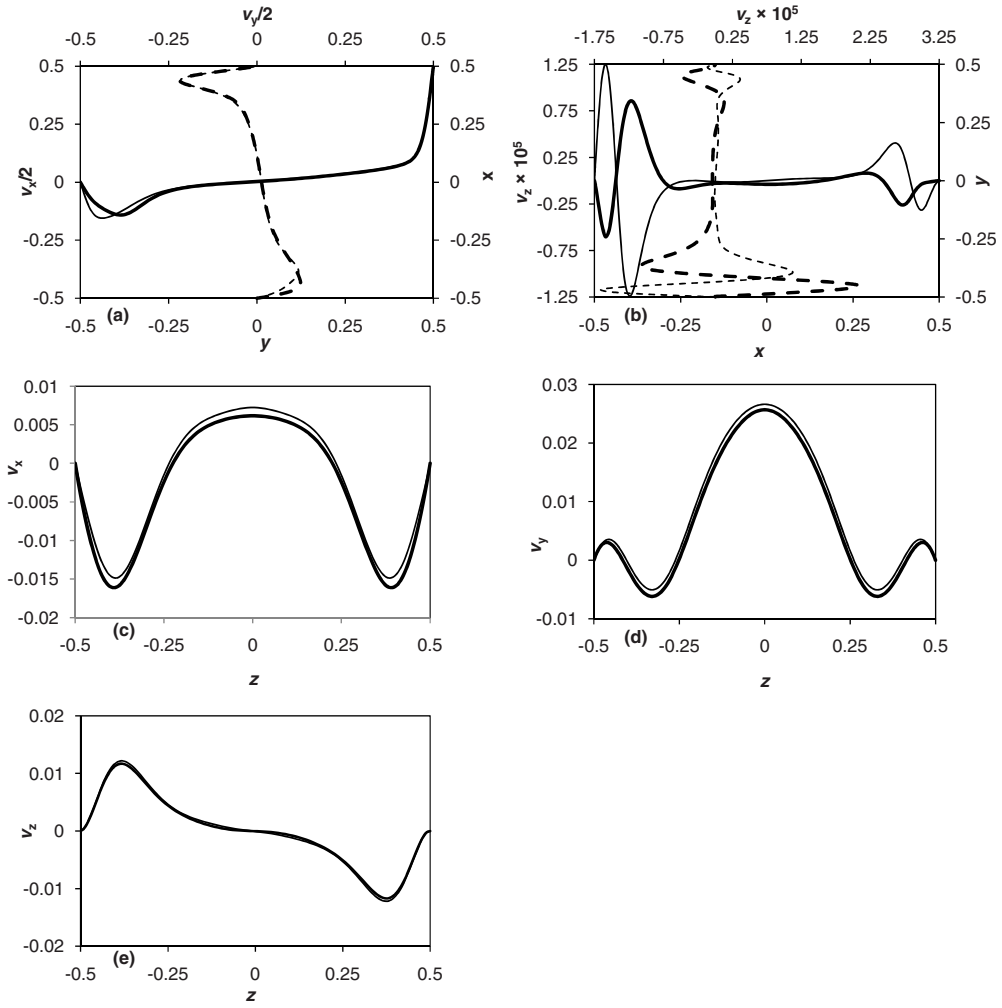

FIG. 9. Typical velocity profiles corresponding to maximal (bold line) and minimal (regular line) values of the total kinetic energy E_k: frames (a) and (b) show the profiles along the centerlines $(x,0,0)$ and $(0,y,0)$; frames (c)–(e): along the centerline $(0,0,z)$.

vortex and lower secondary vortices, while in the case of 2D instability, the largest oscillation amplitudes are observed between the main and upper secondary vortex.

Isosurfaces of oscillation amplitudes of the three velocity components are presented in Fig. 11 for developed oscillatory flow at Re=1970. The amplitudes correspond to the maximum absolute value of the velocity components attained at each grid point over several oscillation periods. The isosurfaces confine the areas at which amplitude values are not less than 25% of the maximal amplitude of the corresponding velocity component. As expected, the spatial pattern of the amplitude values is reflection symmetric with respect to the cavity midplane $z=0$, where amplitudes are the largest. In agreement with the snapshots shown in Fig. 8, the largest amplitudes are observed near the $x=-0.5$ boundary. The three-dimensional amplitude patterns are similar to those reported by Theofilis *et al.*[31] and Chicheportiche *et al.*[35] for a 3D lid-driven box with periodic spanwise boundaries (cf. Fig. 8 of Ref. 31 with Fig. 4 of Ref. 35). The observed similarity suggests that both models with either no-slip and spatially periodic spanwise boundaries are due to the same instability mechanism. At the same time we observe decay of the amplitudes when approaching the no-slip spanwise

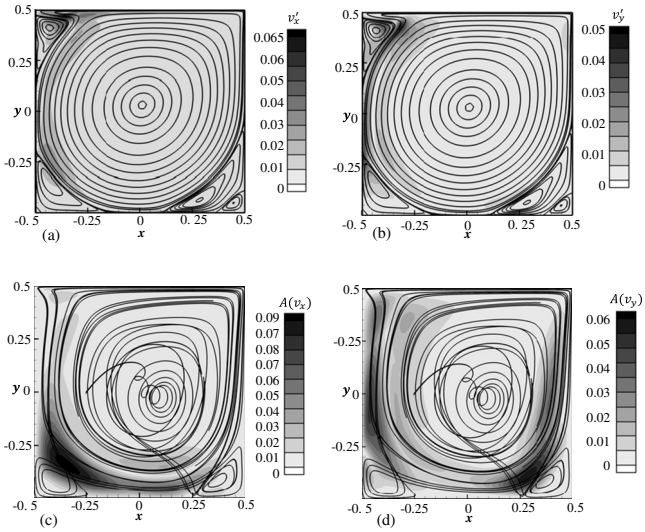

FIG. 10. Instability onset in two- and three-dimensional flows. Streamlines and absolute values of perturbations for Re=8700, two-dimensional flow, 104^2 grid: v_x' (a) and v_y' (b). Trajectories projected on the cavity midplane for Re=1970, three-dimensional flow, 104^3 grid and oscillations amplitude: v_x (c) and v_y (d).

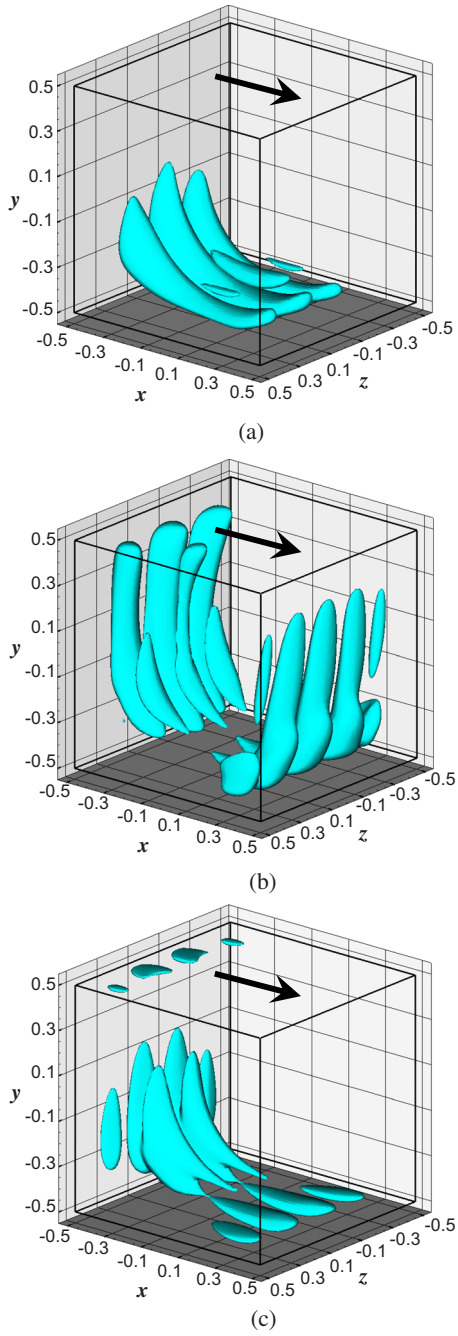

FIG. 11. (Color online) Isosurface of oscillations amplitude, 104^3 grid, Re =1970: (a) v_x component; (b) v_y component; (c) spanwise v_z component. The lid motion is indicated by the arrow.

boundaries (Fig. 11), which is a result of the increasing viscous damping. This additional viscous damping leads to the flow stabilization, so that the critical Reynolds number is approximately twice that of the periodic boundary condition model.

As mentioned above the transition from steady to oscillatory flow is followed by symmetry-breaking with respect to the cavity midplane. This is illustrated in Fig. 12 showing the time evolution of v_z component at the midplane point $(-0.391, 0.395, 0)$. In a subcritical state, at Re=1900, the decaying oscillations eventually converge to zero, thus indicating that in a stable steady regime there is no flow though

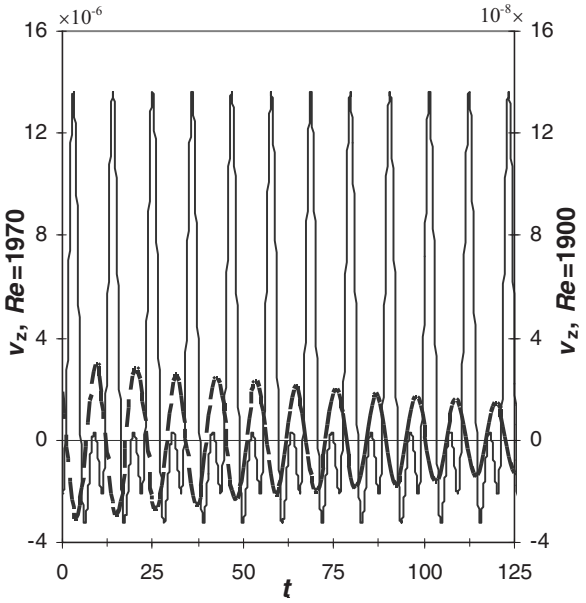

FIG. 12. Time evolution of v_z component at control point $(-0.391, 0.395, 0)$ for Re=1970: continuous line; Re=1900: bold dashed line.

the midplane. In a supercritical state, at Re=1970, we observe not only oscillations of v_z, showing that the flow through the midplane takes place, but also a nonzero average value of these oscillations. The latter means that after the abrupt steady-oscillatory subcritical transition, at the Reynolds number slightly above the critical, the resulting time-averaged flow is also asymmetric. Since the amplitude of the resulting oscillatory flow is finite, this asymmetry may be a nonlinear effect.

V. CONCLUSIONS

The transition from steady to oscillatory state of the lid-driven flow in a cubic cavity was studied by time-dependent three-dimensional computations on three successive grids of 104^3, 152^3, and 200^3 nodes. Grid-independence of the results was established. It was shown that in the stable steady subcritical regimes, the flow remains symmetric with respect to the midplane with no cross-flow through it. At the same time we have argued that the steady three-dimensional flow differs from the corresponding two-dimensional one even at the midplane, and showed that close to the midplane, fluid particles attain the third velocity component.

The present time-dependent computations showed that the oscillatory instability of the lid-driven flow in a cube with the no-slip walls takes place at $\mathrm{Re}_{cr} \approx 1914$ with a dimensionless frequency $\omega_{cr}=0.575$. The value of the critical Reynolds number is estimated via Richardson extrapolation and is expected to be correct to three decimal places. The three reported digits of the frequency value remained unchanged for all the grids considered. Based on the observed single-frequency decaying oscillations in the subcritical regime, an abrupt transition to a finite oscillation amplitude with a slow increase of the Reynolds number, and persistent oscillations observed after the Reynolds number was decreased from supercritical to subcritical values, we argued

that the instability sets in via a subcritical Hopf bifurcation. It was also observed that the transition from steady to oscillatory state is followed by a breaking of the symmetry with respect to the cavity midplane.

ACKNOWLEDGMENTS

This research was supported by Ministry of Science and Technology, Israel, Grant Nos. 3-4293 and 3-5689. We are grateful to the Leibniz-Institute for Crystal Growth for giving us the chance to run the calculations on the HLRN-II supercomputer (see www.hlrn.de).

[1] U. Ghia, K. N. Ghia, and C. T. Shin, "High-Re solutions for incompressible flow using Navier–Stokes equations and a multigrid method," J. Comput. Phys. **48**, 387 (1982).
[2] R. Schreiber and H. B. Keller, "Driven cavity flows by efficient numerical techniques," J. Comput. Phys. **49**, 310 (1983).
[3] O. R. Burggraf, "Analytical and numerical studies of the structure of steady separated flows," J. Fluid Mech. **24**, 113 (1966).
[4] F. Pan and A. Acrivos, "Steady flows in rectangular cavities," J. Fluid Mech. **28**, 643 (1967).
[5] J. R. Koseff, R. L. Street, P. M. Gresho, C. D. Upson, J. A. C. Humphrey, and W. M. To, "A three-dimensional lid-driven cavity flow: Experiment and simulation," *Proceedings of Third International Conference on Numerical Methods in Laminar and Turbulent Flow*, Seattle, WA, edited by C. Taylor (Pineridge Press, Swansea, Wales, Great Britain, 1983), p. 564.
[6] C. J. Freitas, R. L. Street, A. N. Findikakis, and J. R. Koseff, "Numerical simulation of three-dimensional flow in a cavity," Int. J. Numer. Methods Fluids **5**, 561 (1985).
[7] O. Botella and R. Peyret, "Benchmark spectral results on the lid-driven cavity flow," Comput. Fluids **27**, 421 (1998).
[8] A. Yu. Gelfgat, "Implementation of arbitrary inner product in the global Galerkin method for incompressible Navier–Stokes equations," J. Comput. Phys. **211**, 513 (2006).
[9] G. D. Davis and G. D. Mallinson, "An evaluation of upwind and central difference approximations by a study of recirculating flow," Comput. Fluids **4**, 29 (1976).
[10] K. Goda, "A multistep technique with implicit difference schemes for calculating two- or three-dimensional cavity flows," J. Comput. Phys. **30**, 76 (1979).
[11] J. R. Koseff and R. L. Street, "On end wall effects in alid-driven cavity flow," J. Fluids Eng. **106**, 385 (1984).
[12] H. C. Ku, R. S. Hirsh, and T. D. Taylor, "A pseudospectral method for solution of the three-dimensional incompressible Navier–Stokes equations," J. Comput. Phys. **70**, 439 (1987).
[13] A. B. Cortes and J. D. Miller, "Numerical experiments with the lid-driven cavity flow problem," Comput. Fluids **23**, 1005 (1994).
[14] V. Babu and S. A. Korpela, "Numerical solutions for incompressible, three-dimensional Navier–Stokes equations," Comput. Fluids **23**, 675 (1994).
[15] M. M. T. Wang and T. W. H. Sheu, "An element-by-element BICGSTAB iterative method for three-dimensional steady Navier–Stokes equations," J. Comput. Appl. Math. **79**, 147 (1997).
[16] R. Iwatsu, K. Ishii, and J. M. Kuwahara, "Hyun numerical simulation of three dimensional flow structure in a driven cavity," Fluid Dyn. Res. **5**, 173 (1989).
[17] T. P. Chiang, W. H. Sheu, and R. R. Hwang, "Three-dimensional vortex dynamics in a shear-driven rectangular cavity," Int. J. Comput. Fluid Dyn. **8**, 201 (1997).
[18] T. P. Chiang, W. H. Sheu, and R. R. Hwang, "Effect of Reynolds number on the eddy structure in a lid-driven cavity," Int. J. Numer. Methods Fluids **26**, 557 (1998).
[19] T. W. H. Sheu and S. F. Tsai, "Flow topology in a steady three-dimensional lid-driven cavity," Comput. Fluids **31**, 911 (2002).
[20] S. Albensoeder and H. C. Kuhlmann, "Accurate three-dimensional lid-driven cavity flow," J. Comput. Phys. **206**, 536 (2005).
[21] D. Z. Turner, K. B. Nakshatrala, and K. D. Hjelmstad, "A variational multiscale Newton–Schur approach for the incompressible Navier–Stokes equations," Int. J. Numer. Methods Fluids **62**, 119 (2010).
[22] D. L. Sun, Z. G. Qu, Y. L. He, and W. Q. Tao, "Performance analysis of IDEAL algorithm for three-dimensional incompressible fluid flow and heat transfer problems," Int. J. Numer. Methods Fluids **61**, 1132 (2009).
[23] J. W. Goodrich, K. Gustafson, and K. Halasi, "Hopf bifurcation in the driven cavity," J. Comput. Phys. **90**, 219 (1990).
[24] J. Shen, "Hopf bifurcation of the unsteady regularized driven cavity flow," J. Comput. Phys. **95**, 228 (1991).
[25] F. Auteri, N. Parolini, and L. Quartapelle, "Numerical investigation on the stability of singular driven cavity flow," J. Comput. Phys. **183**, 1 (2002).
[26] F. Auteri, L. Quartapelle, and L. Vigevano, "Accurate $\omega-\psi$ spectral solution of the singular driven cavity flow," J. Comput. Phys. **180**, 597 (2002).
[27] A. Abouhamza and R. Pierre, "A neutral stability curve for incompressible flows in a rectangular driven cavity," Math. Comput. Modell. **38**, 141 (2003).
[28] N. Ramanan and G. M. Homsy, "Linear stability of lid-driven cavity flow," Phys. Fluids **6**, 2690 (1994).
[29] V. Theofilis "Globally unstable basic flows in open cavities," AIAA Paper No. 2000–1965, 2000.
[30] S. Albensoeder, H. C. Kuhlmann, and H. J. Rath, "Three-dimensional centrifugal-flow instabilities in the lid-driven cavity problem," Phys. Fluids **13**, 121 (2001).
[31] V. Theofilis, P. W. Duck, and J. Owen, "Viscous linear stability analysis of rectangular duct and cavity flows," J. Fluid Mech. **505**, 249 (1999).
[32] M. Deville, T. H. Lê, and Y. Morchisne, *Numerical Simulation of 3-D Incompressible Unsteady Viscous Laminar Flows*, Notes on Numerical Fluid Mechanics Vol. 36 (Vieweg, Braunschweig, 1992).
[33] E. Leriche and S. Gavrilakis, "Direct numerical simulation of the flow in a lid-driven cubical cavity," Phys. Fluids **12**, 1363 (2000).
[34] R. Bouffanais, M. O. Deville, P. F. Fisher, E. Leriche, and D. Weill, "Large-eddy simulation of the lid-driven cubic cavity flow by the spectral element method," J. Sci. Comput. **27**, 151 (2006).
[35] J. Chicheportiche, X. Merle, X. Gloerfelt, and J. C. Robinet, "Direct numerical simulation and global stability analysis of three-dimensional instabilities in a lid-driven cavity," C. R. Mec. **336**, 586 (2008).
[36] S. Albensoeder and H. C. Kuhlmann, "Nonlinear three-dimensional flow in the lid-driven cavity," J. Fluid Mech. **569**, 465 (2006).
[37] B. B. Beya and T. Lili, "Three-dimensional incompressible flow in a two-sided non-facing lid-driven cubical cavity," C. R. Mec. **336**, 863 (2008).
[38] Yu. Feldman and A. Yu. Gelfgat, "On pressure-velocity coupled time-integration of incompressible Navier–Stokes equations using direct inversion of Stokes operator or accelerated multigrid technique," Comput. Struct. **87**, 710 (2009).
[39] B. D. Hassard, N. D. Kazarinoff, and Y.-H. Wan, *Theory and Applications of Hopf Bifurcation*, Mathematics Society Lecture Note Series Vol. 41 (Mathematics Society, London, 1981).
[40] A. Yu. Gelfgat, "Stability of convective flows in cavities: Solution of benchmark problems by a low-order finite volume method," Int. J. Numer. Methods Fluids **53**, 485 (2007).